Available online at www.sciencedirect.com
SCIENCE DIRECT®
International Journal of Heat and Mass Transfer 48 (2005) 1936–1951
International Journal of HEAT and MASS TRANSFER
www.elsevier.com/locate/ijhmt

Transient natural convection of micropolar fluids between concentric and vertically eccentric spheres

Wen Ruey Chen *

Department of Mechanical Engineering, Far East College, 49 Chung Hua Rd., Tainan 744, Taiwan, ROC

Received 7 April 2004; received in revised form 30 November 2004
Available online 9 March 2005

Abstract

Micropolar fluids in transient analysis have been investigated numerically to determine heat transfer by natural convection between concentric and vertically eccentric spheres with specified isothermal boundary conditions. Calculations were carried out systematically for several different eccentricities and a range of Rayleigh numbers to determine the average Nusselt numbers which are affected by the micropolar parameters (F) on the flow and temperature fields. The skin friction stress on the walls has also been studied and discussed. The governing equations, in terms of vorticity, stream function, temperature and angular momentum are expressed in a spherical polar coordinate system. Results were obtained for steady and transient heat-transfer in vertically eccentric spheres at a Prandtl number of 0.7, with the Rayleigh number ranging from 10^3 to 5×10^5, for a radius ratio of 2.0 and eccentricities varying from -0.625 to $+0.625$, and for the value of micropolar parameters are 0, 1 and 5 respectively. Comparisons are attempted between the Newtonian fluid and micropolar fluid.

Keyword: Natural convection

1. Introduction

Natural convection heat transfer of micropolar fluids in a confined enclosure is a research subject of great importance commonly needed in medical, mechanical, chemical and nuclear engineering industries for various applications including the shear force on the blood circulation in the body, heavy casting production processes, the analysis of polymeric fluids flowing into a mold, nuclear reactor design, and many other practical situations. For some engineering applications, such as gyroscopes, the predication of transient temperature distribution, heat transfer rate and shear stress on the spherical wall from initial state to steady state is very important. The microscopic effects arise from the local structure and micromotions of the fluid elements. It is thus highly desirable to understand the micro-rotation and couple stress using micropolar fluids in the convective heat transfer processes, which are associated with time-dependent properties so that suitable conditions for steady and transient flows growth can be developed for various industrial and scientific applications.

As a result, extensive experimental and theoretical work dealing with flow and associated heat transfer characteristics of natural convection in annuli between two isothermal concentric spheres has been reported in the literature. Experimental heat transfer results for

* Tel.: +886 6 5977051; fax: +886 6 5977050.
E-mail address: ruey666@cc.fec.edu.tw

0017-9310/$ - see front matter © 2005 Elsevier Ltd. All rights reserved.
doi:10.1016/j.ijheatmasstransfer.2004.11.018

Nomenclature

B	dimension material parameter, L^2/j
C_f	skin friction coefficient
C_p	specific heat at constant pressure
e	vertical eccentricity
F	dimensionless micropolar parameter, κ/μ
g	local gravitational acceleration
h	heat transfer coefficient
j	micro-inertia density
k	thermal conductivity
L	annular gap, $\bar{r}_o - \bar{r}_i$
N	dimensionless angular velocity
$\overline{N}$	angular velocity
Nu	local Nusselt number, hL/k
$\overline{Nu}$	average Nusselt number, hL/k
Pr	Prandtl number, ν/α
r	dimensionless coordinate, $\bar{r}/L$
$\bar{r}$	radial coordinate
R	dimensionless radial profile of outer sphere, $\overline{R}/L$
$\overline{R}$	radial profile of outer sphere
Ra	Rayleigh number, $g\beta\Delta\overline{T}L^3/\nu\alpha$
R^*	radius ratio, r_o/r_i
t	time
T	dimensionless temperature, $(\overline{T} - \overline{T}_o)/(\overline{T}_i - \overline{T}_o)$
$\overline{T}$	temperature
v	velocity
V	dimensionless velocity, vL/α

Greek symbols

α	thermal diffusivity
β	thermal expansion coefficient
γ	spin-gradient viscosity
$\Delta\overline{T}$	temperature difference between spheres, $\overline{T}_i - \overline{T}_o$
ε	dimensionless vertical eccentricity, e/L
η	radial coordinate in transformed plane, $(r - r_i)/(r_o - r_i)$
θ	dimensionless angular coordinate, $\bar{\theta}/\pi$
$\bar{\theta}$	angular coordinate
θ^*	angular position at vortex center
κ	vortex viscosity
λ	dimensionless material parameter, $\gamma/j\mu$
μ	dynamic viscosity
ν	kinematic viscosity
ρ	fluid density
τ	dimensionless time, $t\alpha/L^2$
ψ	dimensionless stream function, $\bar{\psi}/\alpha L$
$\bar{\psi}$	stream function in spherical coordinates
ω	dimensionless vorticity, $\bar{\omega}L^2/\alpha$
$\bar{\omega}$	vorticity

Subscripts

i, o	inner and outer
max	maximum

isothermal concentric spheres, the inner being hotter, have been obtained in Ref. [1] for air, in Ref. [2] for water and silicone oils. Semi-analytical studies of the problem have been done in Refs. [3,4]. Numerical results have been reported in Refs. [5,6] for radius ratios up to 2.0 in their investigations. In Ref. [7], a numerical solution for transient natural convection with a large range of Rayleigh number has been computed. Numerical results for transient natural convection between eccentric spheres have been reported in Refs. [8,9].

As far as a micropolar fluid is concerned, the theory was in sequence developed by Eringen [10–12], in which the local effects resulting from microstructure and gyration motions of the fluid elements were taken into consideration. The non-Newtonian behavior of liquid crystals, ferro liquids and polymeric fluids were being studied at many researchers. A detailed review made by Ariman et al. [13] demonstrated that for linear, viscous, and isotropic fluids the non-Newtonian behavior of the above mentioned liquids can be modeled by the micropolar fluid theory. The effect of microstructure on the thermal convection in a rectangular box of fluid heated from below, was analyzed by Jena and Bhattacharyya [14], who revealed that the dimensionless parameters vortex viscosity and micropolar heat conduction are important to the onset of convection. There are only few studies investigating the effect of microstructure on the free convection heat transfer in spherical annuli.

To further extend the existing knowledge on natural convection heat transfer of micropolar fluids in spherical enclosures, this study considers the laminar transient natural convection in concentric and eccentric spherical annuli with isothermal boundary conditions. A finite difference solution is obtained for the governing equations in terms of stream function, vorticity, angular momentum and energy in a spherical polar coordinate system. The effects of eccentricity, Rayleigh number, and fluid property on the flow fields and heat transfer characteristics are discussed respectively. The details of the method are described in the next section. We wish to point out that our formulations were represented by general form for various natural convection problems involving concentric and vertically eccentric spheres.

2. Mathematical formulation

The geometric configuration of the physical system is a concentric or vertically eccentric arrangement of two circular spheres of radii r_o and r_i located at O′ and O, respectively. The eccentricity of the outer sphere is measured by the distance ε. If the outer sphere is placed above the central position, ε has a positive value, otherwise ε is negative. For a natural convective heat transfer problem, the largest heat transfer variation due to eccentricity occurs when the direction of ε is aligned with the gravitational direction. Therefore, this study focuses on the problem that ε is vertically shifted.

The space between the inner and outer spheres is filled with a viscous and incompressible micropolar fluid. Initially, the annulus is at a uniform temperature T_o, and a quiescent state is assumed, while the temperature of the inner sphere is suddenly changed to a higher temperature T_i and the outer sphere is maintained at T_o. The heat transfer takes place between the spheres by natural convection. A model to describe the process has been derived making the following assumptions: (1) the flow within the annulus is laminar, (2) all fluid properties, are taken to be constant, except for the density variation with temperature in the buoyancy term, i.e. the Boussinesq approximation is valid, (3) the flow is symmetrical about the vertical axis which is parallel to the line of gravity acceleration, (4) viscous dissipation and radiation effects are neglected.

A spherical polar coordinate system (r, θ, φ) and grids system were chosen as shown in Fig. 1. To deal with the numerical formulation associated with the complex physical domain of the vertically eccentric annulus, a radial coordinate transformation is adopted to map the eccentric annular gap into a unit sphere. The outer sphere radius $r = R(\theta)$ is transformed into the unit sphere $\eta = 1$, while the inner sphere radius $r = r_i$ is transformed into the pole $\eta = 0$. This transformation is obtained by defining a new radial coordinate as

$$\eta = \frac{r - r_i}{R(\theta) - r_i} \tag{1}$$

where $R(\theta)$ denotes variable dimensionless profile of the outer sphere measured from the center of the inner sphere, which is symmetric with respect to the vertical axis in any angular position of φ-direction and is expressed by

$$R(\theta) = \sqrt{r_o^2 - \varepsilon^2 \sin\theta} - \varepsilon\cos\theta \tag{2}$$

The governing equations for the two-dimensional problem in dimensionless terms can be written as

Vorticity transport equation:

$$\begin{aligned}\frac{\partial\omega}{\partial\tau} &+ \frac{1}{\pi r^2\sin(\pi\theta)}\left\{\left(\frac{\partial\eta}{\partial r}\right)\cdot\left[\frac{\partial\psi}{\partial\eta}\frac{\partial\omega}{\partial\theta} - \frac{\partial\psi}{\partial\theta}\frac{\partial\omega}{\partial\eta}\right]\right.\\ &\left. + \left[\left(\frac{1}{r}\frac{\partial\eta}{\partial\theta} - \pi\cot(\pi\theta)\frac{\partial\eta}{\partial r}\right)\frac{\partial\psi}{\partial\eta} + \frac{1}{r}\frac{\partial\psi}{\partial\theta}\right]\omega\right\}\\ &= Pr(1+F)\left[\nabla_1^2 - \frac{1}{r^2\sin^2(\pi\theta)}\right]\omega\\ &\quad + Pr\cdot F\left[\nabla_1^2 - \frac{1}{r^2\sin^2(\pi\theta)}\right]N\\ &\quad - Pr\cdot Ra\left[\left(\sin(\pi\theta)\frac{\partial\eta}{\partial r} + \frac{\cos(\pi\theta)}{\pi r}\frac{\partial\eta}{\partial\theta}\right)\frac{\partial T}{\partial\eta}\right.\\ &\quad \left. + \frac{\cos(\pi\theta)}{\pi r}\frac{\partial T}{\partial\theta}\right]\end{aligned} \tag{3}$$

Stream function equation:

$$D_1^2\psi = \omega r\sin(\pi\theta) \tag{4}$$

Angular momentum equation:

$$\begin{aligned}\frac{\partial N}{\partial\tau} &+ \frac{1}{\pi r^2\sin(\pi\theta)}\left\{\left(\frac{\partial\eta}{\partial r}\right)\left[\frac{\partial\varphi}{\partial\eta}\frac{\partial N}{\partial\theta} - \frac{\partial\varphi}{\partial\theta}\frac{\partial N}{\partial\eta}\right]\right.\\ &\left. + \left[\left(\frac{1}{r}\frac{\partial\eta}{\partial\theta} - \pi\cot(\pi\theta)\frac{\partial\eta}{\partial r}\right)\frac{\partial\varphi}{\partial\eta} + \frac{1}{r}\frac{\partial\varphi}{\partial\theta}\right]N\right\}\\ &= Pr\cdot F\cdot B(\omega - 2N) + Pr\cdot\lambda\left(\nabla_1^2 - \frac{1}{r^2\sin^2\theta}\right)N\end{aligned} \tag{5}$$

Energy equation:

$$\frac{\partial T}{\partial\tau} + \frac{1}{\pi r^2\sin(\pi\theta)}\frac{\partial\eta}{\partial r}\left(\frac{\partial\psi}{\partial\eta}\frac{\partial T}{\partial\theta} - \frac{\partial\psi}{\partial\theta}\frac{\partial T}{\partial\eta}\right) = \nabla_1^2 T \tag{6}$$

Skin-friction coefficient

$$C_f = \frac{2\tau_w}{\rho(\alpha/L)^2} = Pr(2+F)\left[r\frac{\partial}{\partial r}\left(\frac{V_\theta}{r}\right) + \frac{1}{r}\frac{\partial V_r}{\partial\theta}\right] \tag{7}$$

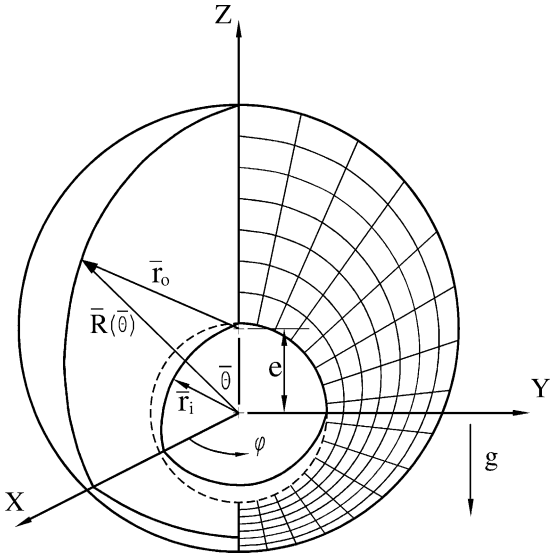

Fig. 1. Coordinate and grids system for spherical annulus.

where

$$\frac{\partial \eta}{\partial r} = \frac{1}{R(\theta) - r_i} \tag{8}$$

$$\frac{\partial \eta}{\partial \theta} = \frac{-\eta}{R(\theta) - r_i} \frac{\partial R(\theta)}{\partial \theta} \quad (\text{if } \varepsilon = 0, \text{ then } R(\theta) = r_o) \tag{9}$$

$$\frac{\partial^2 \eta}{\partial \theta^2} = \frac{-1}{R(\theta) - r_i} \left(\eta \frac{\partial^2 R(\theta)}{\partial \theta^2} + 2 \frac{\partial \eta}{\partial \theta} \frac{\partial R(\theta)}{\partial \theta} \right) \tag{10}$$

$$\begin{aligned} \nabla_1^2 = & \left[\left(\frac{\partial \eta}{\partial r} \right)^2 + \frac{1}{\pi^2 r^2} \left(\frac{\partial \eta}{\partial \theta} \right)^2 \right] \frac{\partial^2}{\partial \eta^2} \\ & + \left[\frac{2}{\pi^2 r^2} \left(\frac{\partial \eta}{\partial \theta} \right) \right] \frac{\partial^2}{\partial \eta \, \partial \theta} + \left[\frac{1}{\pi^2 r^2} \right] \frac{\partial^2}{\partial \theta^2} \\ & + \left[\frac{2}{r} \left(\frac{\partial \eta}{\partial r} \right) + \frac{1}{\pi^2 r^2} \left(\frac{\partial^2 \eta}{\partial \theta^2} \right) + \frac{\cot(\pi\theta)}{\pi r^2} \left(\frac{\partial \eta}{\partial \theta} \right) \right] \frac{\partial}{\partial \eta} \\ & + \left[\frac{\cot(\pi\theta)}{\pi r^2} \right] \frac{\partial}{\partial \theta} \end{aligned} \tag{11}$$

$$\begin{aligned} D_1^2 = & \left[\left(\frac{\partial \eta}{\partial r} \right)^2 + \frac{1}{\pi^2 r^2} \left(\frac{\partial \eta}{\partial \theta} \right)^2 \right] \frac{\partial^2}{\partial \eta^2} \\ & + \left[\frac{2}{\pi^2 r^2} \left(\frac{\partial \eta}{\partial \theta} \right) \right] \frac{\partial^2}{\partial \eta \, \partial \theta} + \left[\frac{1}{\pi^2 r^2} \right] \frac{\partial^2}{\partial \theta^2} \\ & + \left[\frac{1}{\pi^2 r^2} \left(\frac{\partial^2 \eta}{\partial \theta^2} \right) - \frac{\cot(\pi\theta)}{\pi r^2} \left(\frac{\partial \eta}{\partial \theta} \right) \right] \frac{\partial}{\partial \eta} \\ & - \left[\frac{\cot(\pi\theta)}{\pi r^2} \right] \frac{\partial}{\partial \theta} \end{aligned} \tag{12}$$

The associated initial and boundary conditions for the problem considered are

for $\tau = 0$

$$T = 0, \quad \omega = \psi = N = 0, \quad \frac{\partial \psi}{\partial \eta} = \frac{\partial \psi}{\partial \theta} = 0, \quad \text{everywhere} \tag{13}$$

for $\tau > 0$

at $\eta = 0$,

$$\psi = \frac{\partial \psi}{\partial \eta} = 0, \quad T = 1, \quad \omega = \frac{1}{r_i \sin(\pi\theta)} \left(\frac{\partial \eta}{\partial r} \right)^2 \frac{\partial^2 \psi}{\partial \eta^2}, \quad N = \frac{1}{2}\omega \tag{14}$$

at $\eta = 1$,

$$\psi = \frac{\partial \psi}{\partial \eta} = 0, \quad T = 0, \quad \omega = \frac{1}{r_o \sin(\pi\theta)} \left[\left(\frac{\partial \eta}{\partial r} \right)^2 + \frac{1}{\pi^2 r^2} \left(\frac{\partial \eta}{\partial \theta} \right)^2 \right] \frac{\partial^2 \psi}{\partial \eta^2}, \quad N = \frac{1}{2}\omega \tag{15}$$

at $\theta = 0, 1$,

$$\psi = \omega = N = \frac{\partial T}{\partial \theta} = 0 \tag{16}$$

From the above formulation, the governing parameters for the present problem are the Rayleigh number Ra, the Prandtl number Pr, the radius ratio R^*, the material parameter B, the micropolar parameter F and the eccentricity ε.

The local and average Nusselt number at inner and outer radii are defined as:

$$Nu_{i,o} = -\frac{1}{r_i r_o} \left[r^2 \frac{\partial \eta}{\partial r} \frac{\partial T}{\partial \eta} \right]_{\eta = 0,1} \tag{17}$$

$$\overline{Nu} = -\pi \int_0^1 Nu_{i,o} \left[\frac{\sin(\pi\theta)}{2} \right] d\theta \tag{18}$$

3. Numerical method

To solve the problem, the governing equations as well as initial and boundary conditions were discritized by the finite difference method. Eqs. (3)–(6) expressing the vorticity transport, streamfunction, angular momentum and energy transport equations, together with initial and boundary conditions in Eqs. (13)–(16), provide a complete description of the problem. Since the flow is known to be parabolic in time but elliptic in space, the solution for the problem can only be marched in time. In this study, the time-dependent vorticity, angular momentum transport and energy transport equations were solved by employing the alternating direction implicit (ADI) finite technique [15,16], while the stream function equation was solved by employing the successive over-relaxation (SOR) technique [17,18]. The first and second derivatives in space were approximated by central difference while the time derivatives were approximated by forward difference. Derivative at the boundaries were approximated by a three point forward or backward difference. The results presented in this article are all obtained by using a mesh of 41×41 cells. Numerical test calculations were also performed for different time step sizes. Two different time step sizes depending on the geometry, have been used for the calculations: 1×10^{-4} for $\varepsilon = 0.0$ and 5×10^{-5} for $\varepsilon = \pm 0.625$.

The solution was considered convergent when the relative error between the new and old values of the field variables Φ during every time step was less than a prescribed criterion (10^{-4}), where Φ represents ω, ψ, N and T.

$$\frac{|\Phi_{new} - \Phi_{old}|_{max}}{|\Phi_{new}|_{max}} \leqslant 10^{-4} \tag{19}$$

Further, the steady-state solution was determined by requiring the relative error between the present and next time step values of all field variables for the inner and outer spheres to be:

$$\frac{|\Phi^{n+1}-\Phi^{n}|_{\max}}{|\Phi^{n+1}|_{\max}} \leqslant 10^{-4} \tag{20}$$

where the superscripts n and $(n+1)$ indicate the nth and $(n+1)$st time step, respectively.

4. Results and discussion

Numerical calculations have been performed systematically for a spherical annulus of radius ratio fixed at 2.0, the Prandtl number fixed at 0.7 and the material parameters fixed at $B = 1$ and $\lambda = 1$. The Rayleigh numbers ranging from 10^3 to 5.0×10^5, the eccentricities varying from -0.625 to $+0.625$ and the micropolar parameters using with $F = 0$, 1 and 5 respectively, where $F = 0$ is the micropolar fluid model in the limiting case, which is equivalent to the problem of Newtonian fluid. It is convenient to checking the validity of the numerical results. The numerical results are verified by comparing the present results with those of earlier worker [3–8]. Table 1 compares the present calculated results with earlier workers [3–8]. The heat-transfer results are in excellent agreement with the finding of authors [7,8]. It was depicted by the average Nusselt number vs. Rayleigh as shown in Fig. 11.

Fig. 2(a) shows an evolution of streamlines and isotherms for a Rayleigh number of 10^3. Fig. 2(b) presents a corresponding evolution for a Rayleigh number of 10^5. This evolution of results is designed to demonstrate the effects of Rayleigh number (Ra) and micropolar parameter (F) on the heat and fluid flow patterns in the concentric annulus. Because the problem is symmetric to the axis, each annulus contains the isotherms on the left and streamlines on the right. To facilitate the comparison of different configurations, the number of contours within each geometric structure is kept constant at nine for temperature and at six for stream function. Since the inner sphere is kept hotter, the hot fluid near the inner sphere rises upward due to thermal expansion. The uprising plume is then cooled by the colder fluid near the upper part of outer sphere. The colder and denser fluid will eventually flow downward along the surface of the outer sphere.

About the low value of Rayleigh number of $Ra = 10^3$ in Fig. 2(a), as micropolar parameter (F) increases, it is found that the position of vortex center of the eddy shifts downward along the annular space while the maximum value of the stream function also decreases. When the value of micropolar parameter $F = 5$ shows that the maximum value of stream function $\psi_{\max} = 0.710$ with the angular position of vortex center of the crescent-shaped lies at $\theta^* = 90.0°$ from the upper vertical line symmetry about midgap position. At $Ra = 10^5$, as shown in Fig. 2(b), the fluid motion becomes stronger, as indicated by the increased absolute value of the stream function and the vortex center of the eddy shifted upward. Examination of the isothermal patterns also reveals that laminar convection was the dominant mode of heat transfer; on the contrary, the pseudoconduction heat transfer regime appeared in Fig. 2(a). Simultaneously, the maximum value of the stream function decreases with the increase of micropolar parameter (F).

Table 1
Comparison of the calculated average Nusselt number $\overline{Nu}$, maximum value of stream function $\psi_{\max}$ and angular position of vortex center θ^* at steady-state, as functions of $R^* = 2.0$, $Pr = 0.7$, $\varepsilon = 0.0$, $F = 0$ and $Ra = 10^3$–5×10^5

Ra		Nu	$\psi_{\max}$	θ^*
1.0×10^3	Present results	1.1003	3.2265	81°
	Mack and Hardee [3]	1.1200	3.2100	77°
	Singh and Chen [4]	1.1200	3.4900	79°
	Astill et al. [5]	1.1010	–	–
	Garg [6]	1.1006	–	–
	Chu and Lee [7]	1.0990	3.2090	81°
	Chiu and Chen [8]	1.1021	3.2360	81°
1.0×10^4	Present results	1.9601	17.3948	67.5°
	Chu and Lee [7]	1.9730	17.2800	67.5°
	Chiu and Chen [8]	1.9110	17.9400	67.5°
1.0×10^5	Present results	3.3851	35.9192	54°
	Chu and Lee [7]	3.4890	36.5300	54°
	Chiu and Chen [8]	3.3555	35.9240	54°
5.0×10^5	Present results	4.9147	52.5188	49.5°
	Chu and Lee [7]	5.3780	53.4200	49.5°
	Chiu and Chen [8]	4.8657	–	–

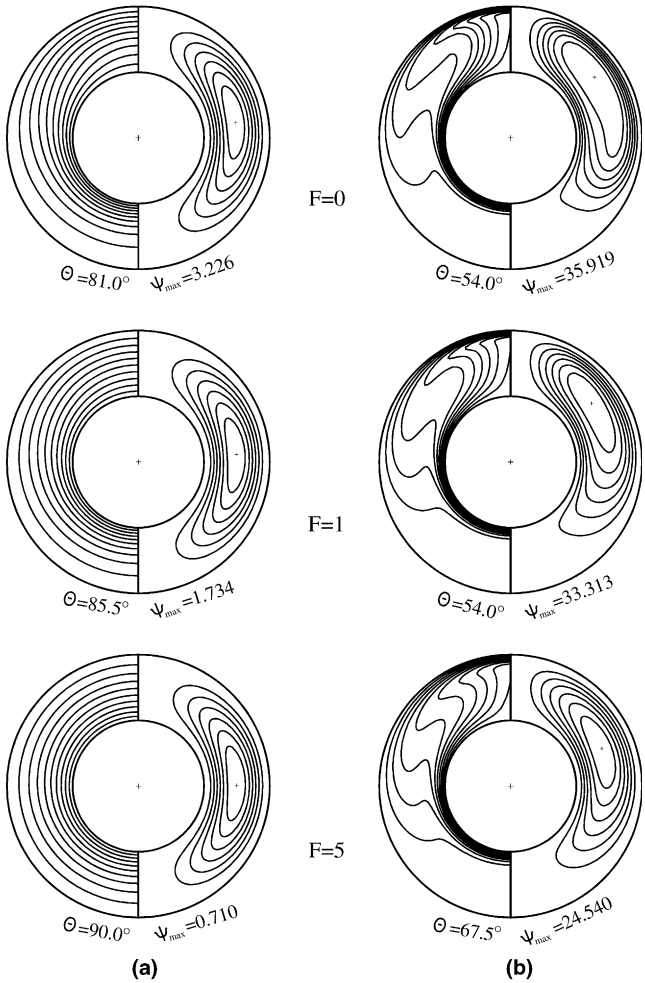

Fig. 2. Isotherms (left) and streamlines (right) for $R^* = 2.0$, $Pr = 0.7$ and $\varepsilon = 0.0$ at different micropolar parameters $F = 0$, 1, 5: (a) $Ra = 10^3$; (b) $Ra = 10^5$.

About the high value of Rayleigh number of $Ra = 10^5$ in Fig. 3(a) and (b), which illustrate that the streamline and isotherm distributions at the various micropolar parameters (F) for positive and negative eccentricity, respectively. For positive eccentric geometry (Fig. 3(a)) within such favorable configuration for convective motion, the streamline distributions were depicted in the larger feature for the eccentric geometry space. It is evident that the convective flows are both larger and stronger than for those of the concentric annulus (Fig. 2(b)); the maximum value of stream functions were observed to be further pronounced. On the other hand, the negative eccentric geometry provides the least favorable circumstance for the development of natural convection. Then again, we have also observed that the stream function decreases with the increase of micropolar parameter (F) under positive ($e = 0.625$) and negative ($e = -0.625$) eccentricity.

Fig. 4 presents a series of streamline configurations, isotherms and velocity vectors for radius ratio of 2.0, Prandtl number of 0.7, Rayleigh number of 5×10^5, micropolar parameter of 5, and the eccentricity of 0.0; Figs. 5 and 6 present a corresponding series for the eccentricities of 0.625 and -0.625 respectively. The streamlines and isotherms are displayed on the left-hand side while the velocity fields are displayed on the right-hand side. The velocity vectors were normalized by maximum local velocity in the flow fields. At the first time step corresponding to (I), the fluid flow in the annulus, where the vortex center (the position with the maximum value of the stream function) rises to the upper portion and forms a stronger circulation of core region in the clockwise direction, the isotherms quickly distribute near both the upper vertical axis-symmetry and upper outer spherical surface, which implies that the local convective flow on the heat transfer presents this region at

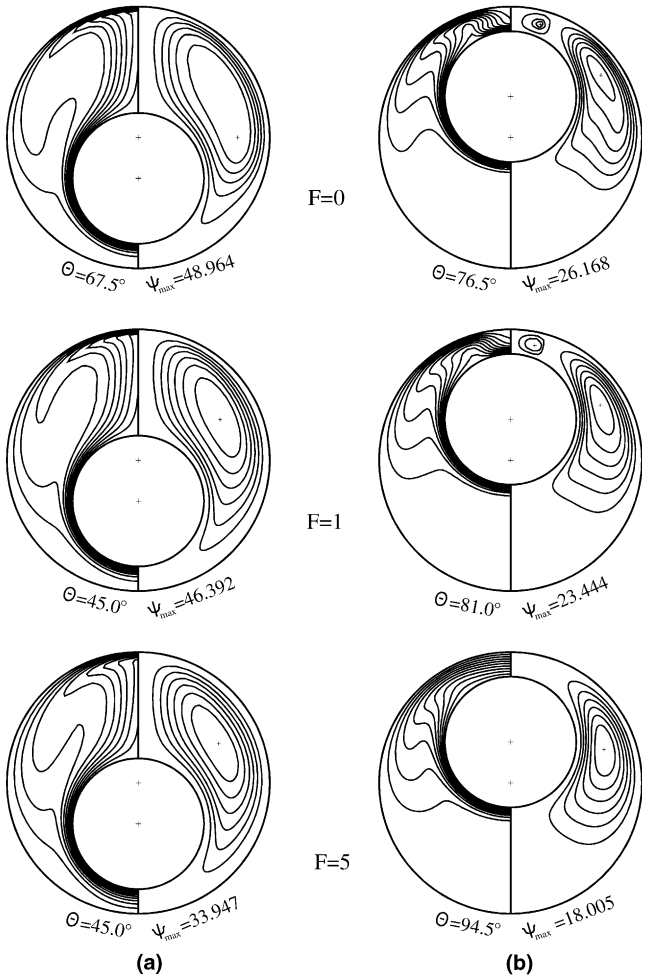

Fig. 3. Isotherms (left) and streamlines (right) for $R^* = 2.0$, $Pr = 0.7$ and $Ra = 10^5$ at different micropolar parameters $F = 0$, 1, 5: (a) $\varepsilon = 0.625$; (b) $\varepsilon = -0.625$.

the earliest, further indicating that the thermal plume above the inner sphere forms concentric rings. When the time step proceeds from (I) to (II), the fluid motion expands and distributes gradually within the annulus region while the buoyant effect increases along inner sphere wall and decreases along outer sphere wall. It is demonstrated that the fluid in the close vicinity of the inner sphere has lower density than that near the outer sphere. Thus, the fluid near the surface of the inner sphere moves upward while the relatively heavy fluid near the outer sphere moves downward; the maximum value of the stream function decreases gradually, and the vortex center of eddy shifts upward above the horizontal axis. When the time step proceed from (II) to (III), the fluid motion within the annulus is wide and uniformly distributed, which implies that the convective effect cause to extend the isothermal downward to the lower symmetric axis along the midgap. The maximum value of the stream function decreases gradually, and the vortex center of eddy shifts upward above the horizontal axis. Finally, during a later time step proceed from (III) to (IV), corresponding to the heat and flow will tend to get a quasi-steady state that the maximum value of stream function $\psi_{\max} = 42.693$ and the angular position of vortex center of the crescent-shaped lies at $\theta^* = 40.5°$ from the upper vertical line symmetry about midgap position.

Next, the isotherms, streamlines and velocity vectors for the eccentric configurations considered in this study are also examined. Figs. 5 and 6 illustrate the transient isotherms, streamlines and velocity vectors at different F for positive and negative eccentricity, respectively. Common to all three geometries considered is the existence of higher temperature gradients as seen at the outer wall at $\theta = 0°$ for higher values of the Rayleigh number when a quasi-steady state is approached. The

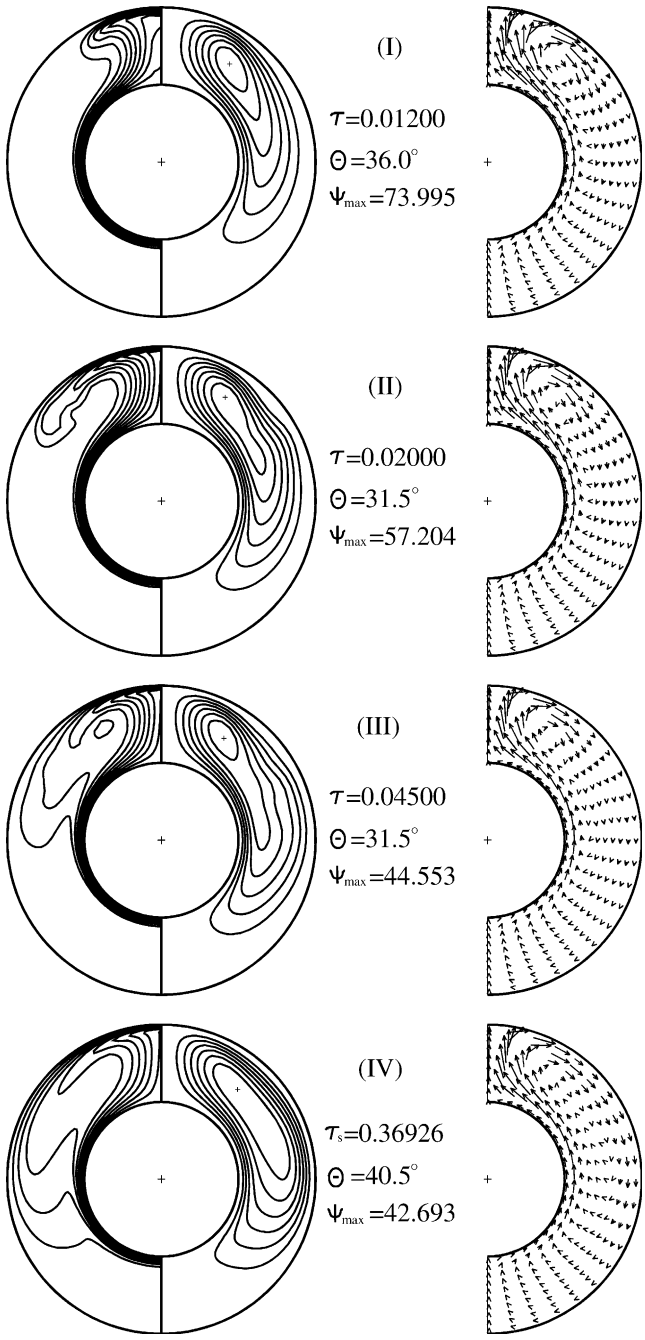

Fig. 4. Isotherms, streamlines, and velocity distributions for $Pr = 0.7$, $Ra = 5 \times 10^5$, $R^* = 2.0$, $F = 5$ and $\varepsilon = 0.0$ at different time steps.

presence of large convection at the higher values of the Rayleigh numbers is demonstrated by the appearance of temperature inversions mainly in the upper half of each annulus. The effect of eccentricity on the flow is revealed by comparing the different eccentricities, the isotherms and streamlines at fixed values of the Rayleigh number, For the positive eccentric geometry in Fig. 5, Within such a favorable configuration for convective motion, it is evident that the convective flows are both larger and stronger than those of for the concentric spheres; the two spheres are very close to each other along $\theta = \pi$ near the lower symmetric axis. In this

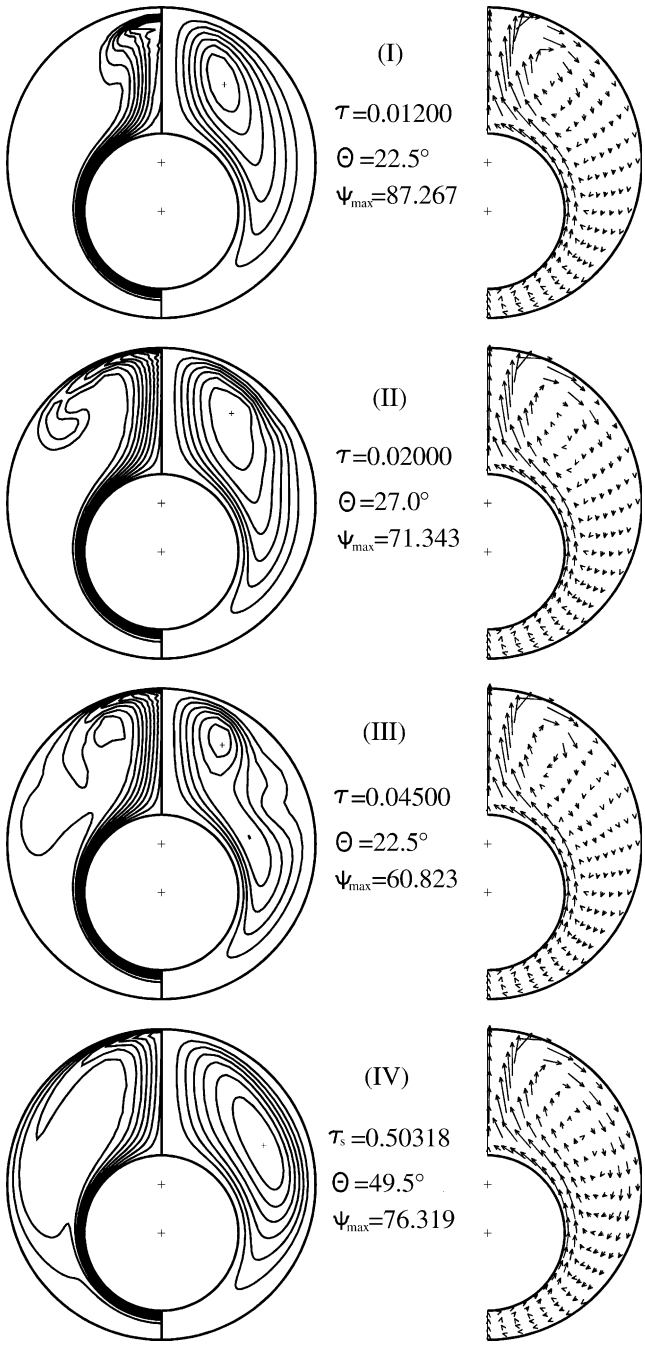

Fig. 5. Isotherms, streamlines, and velocity distributions for $Pr = 0.7$, $Ra = 5 \times 10^5$, $R^* = 2.0$, $F = 5$ and $\varepsilon = 0.625$ at different time steps.

region, the effects of convection are diminished, and the shapes of the isotherms are largely determined by the conductive mode of heat transfer.

The effect of negative eccentric geometry is shown in Fig. 6. Here the convective cell center has moved toward $\theta = \pi$. This cell is also less powerful than that in the concentric case. Clearly, in the top narrow midgap between two spheres inhibits convective motion in the fluid. Thus the isotherms show smaller temperature inversions when compared to the concentric case in Fig. 4. The bottom of the annulus (near $\theta = \pi$) exhibits an enlarged stagnant region of fluid. In each case, the motion of the fluid is

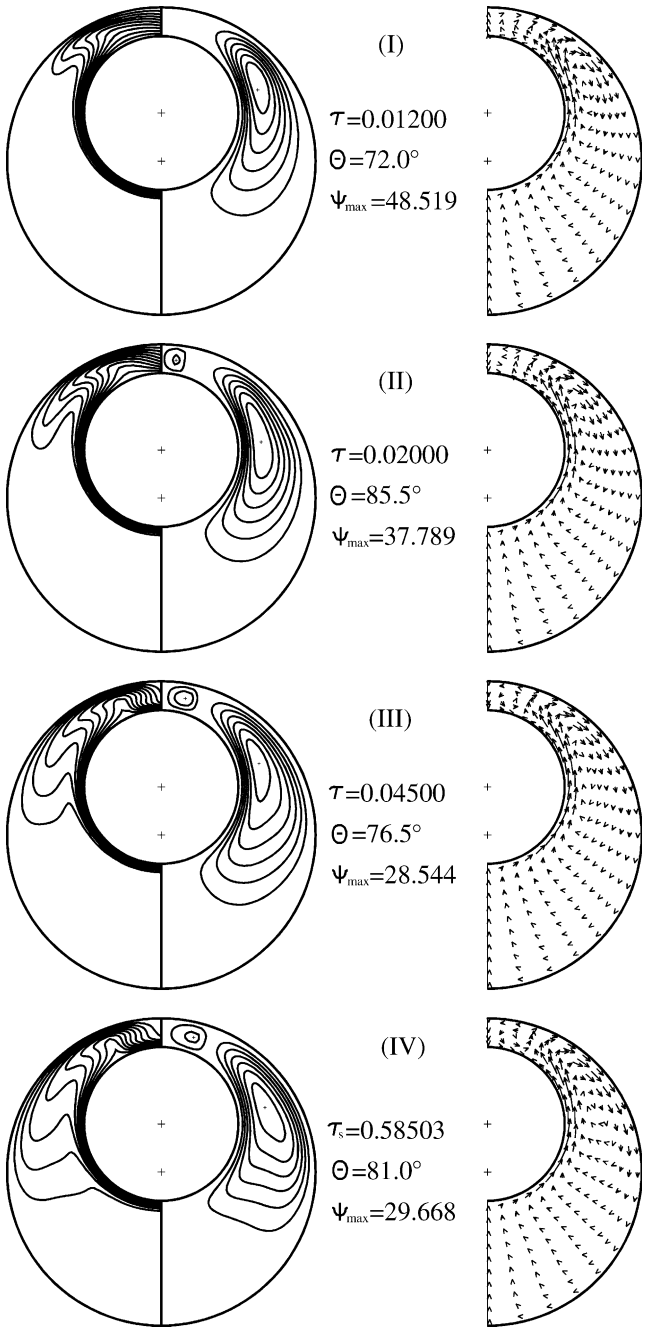

Fig. 6. Isotherms, streamlines, and velocity distributions for $Pr = 0.7$, $Ra = 5 \times 10^5$, $R^* = 2.0$, $F = 5$ and $\varepsilon = -0.625$ at different time steps.

clockwise. The region of almost stagnant fluids exist near $\theta = \pi$, at the lower region, this zone increases in size for the negative eccentricities because of the increased resistance to flow. Since, the negative eccentric geometry provides the least favored circumstance for the development of natural convection. Both the size and strength of the fluid flow are markedly reduced. Moreover, Fig. 6 shows an anti-clockwise rotating secondary cell in the top of the annulus as time step proceeds (II) corresponding to $\tau = 0.02$ while the primary central eddy is clockwise. As the time step arrives at steady state, we find that a multicell flow is predicted in which one

secondary cell having a sense of rotation opposite to that of the primary central eddy is formed. The secondary cell was found near the top of the inner-sphere. These phenomena were similarly stated by Caltagirone et al. [19], who expressed that the muticellular flows occur at critical Rayleigh number for the radius ratio 2.0.

As a result of the difference in streamlines, isotherms and velocity vectors, the local Nusselt number also behaves differently. Figs. 7 and 8 depict the heat flux behavior of the local Nusselt number along the inner and outer spheres of three geometries considered for two values of *Ra*. Examining Fig. 7(a)–(c) and 8(a) and (b), we find that the local Nusselt number on the outer sphere has a peak near the top of the annulus at different micropolar parameters for the concentric, the positive eccentric and negative eccentric annulus at low Rayleigh number. The peak value increases with an increase in Rayleigh number. For the negative eccentricity in Fig. 8(c), the local Nusselt numbers on the inner and outer sphere have minimum and maximum values, respectively. The generation and development with the different micropolar parameters of the maximum and minimum values will be oscillated near $\theta = 30$–$55°$. It is implied that the secondary flow taken place on the top of the annulus is also weak, although the Rayleigh number was increased to 10^5. This secondary cell leads the fluid into a narrow gap being unfavorable convection motion.

Figs. 9 and 10 show the steady skin-friction coefficients $C_{fi,o}$ vary with θ. When compared with that at fixed value of F, it is obvious that both absolute value of $|C_{fi}|$ and $|C_{fo}|$ increase with *Ra* for a given values of

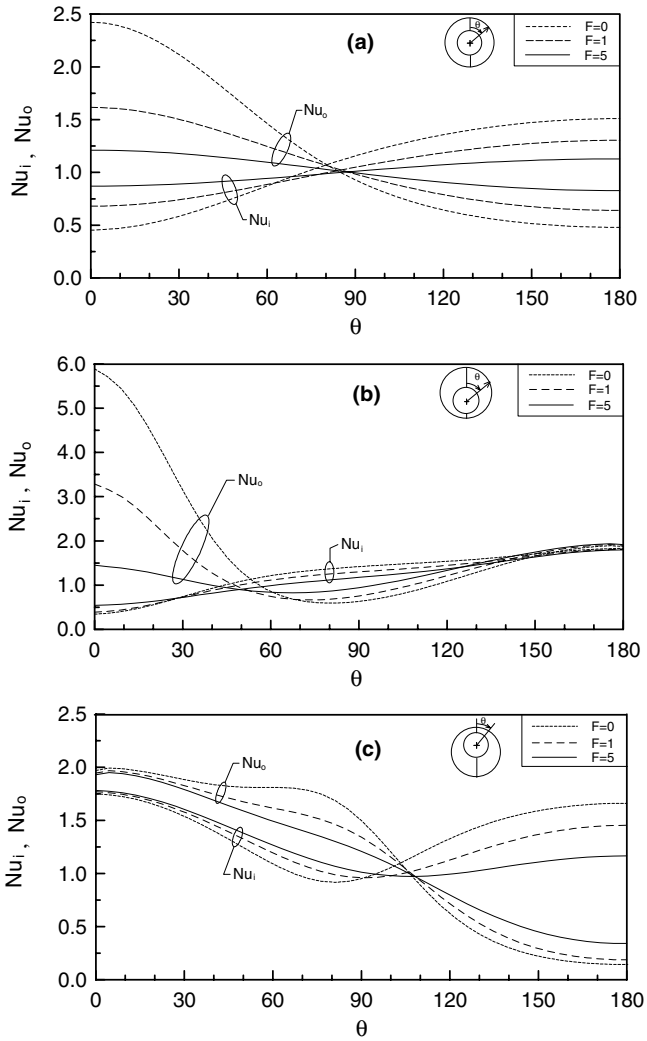

Fig. 7. Local Nusselt numbers distribution on the inner and outer spheres for $R^* = 2.0$, $Pr = 0.7$ and $Ra = 10^3$ at different micropolar parameters $F = 0$, 1, 5: (a) $\varepsilon = 0.0$; (b) $\varepsilon = 0.625$; (c) $\varepsilon = -0.625$.

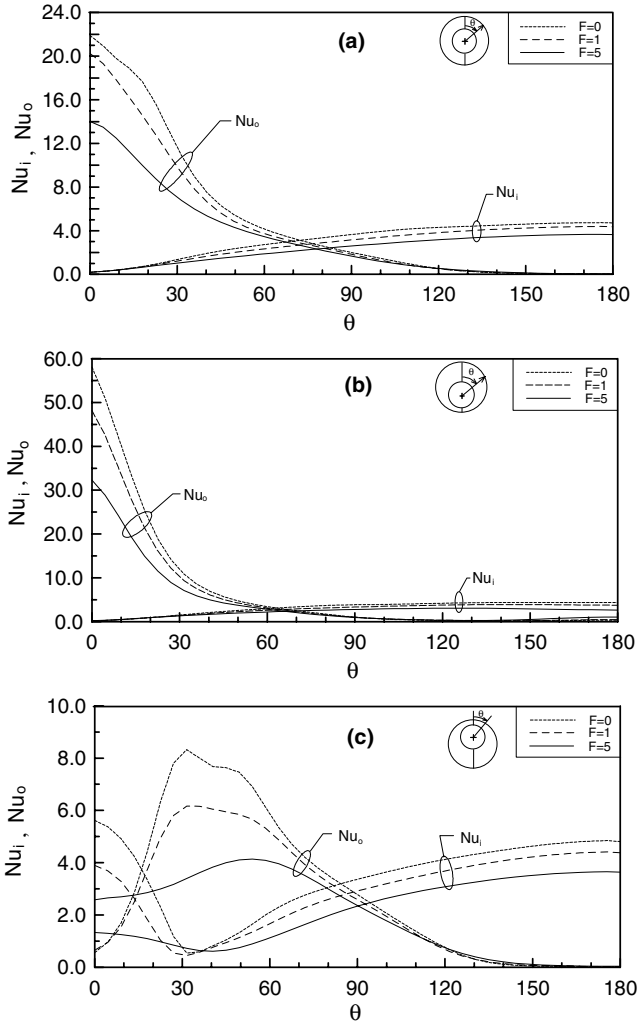

Fig. 8. Local Nusselt numbers distribution on the inner and outer spheres for $R^* = 2.0$, $Pr = 0.7$ and $Ra = 10^5$ at different micropolar parameters $F = 0$, 1, 5: (a) $\varepsilon = 0.0$; (b) $\varepsilon = 0.625$; (c) $\varepsilon = -0.625$.

$R^* = 2.0$ and $Pr = 0.7$. These were to be expected, since the magnitude of buoyant force and hence the strength of the convective cells increase with Ra. Eq. (7) shows that there are two important parameters. They are the velocity gradient and the vortex viscosity that influence the skin-friction coefficient. It reveals that, for a Newtonian fluid, the effect of the velocity gradient on the skin friction coefficient is more pronounced than that of the vortex viscosity, while for a micropolar fluid the opposite is true. Fig. 9 demonstrates a set of typical steady skin-friction coefficient distributions on the spherical surface at fixed low Rayleigh number is 10^3. As F increases, it implies that the vortex viscosity increases for a micropolar fluid. The effect of an absolute value of the skin-friction coefficient $|C_f|$ increases with increase of the vortex viscosity but decreases with weak motion of fluid under low Rayleigh number. Finally, Examining Fig. 9, we see that at any θ position, the total $|C_{fi,o}|$on the spherical wall of the inner and outer spheres almost decreases with increasing F for three different eccentric geometric structures. When the Rayleigh number increases to 10^5, as illustrated in Fig. 10, curiously, the $|C_{fo}|$ does not decrease with increasing F. These trends do not extend to the outer sphere at three geometric eccentric structures under this high Rayleigh number. It implies that the micropolar parameter effect to the value of $|C_{fo}|$ does not regularly comply with the Rayleigh number which was changed. The location of the maximum absolute value of the skin-friction coefficient shifts upward to near $\theta = 25°$ for inner sphere $|C_{fi}|_{max}$ and near $\theta = 85°$ for outer sphere $|C_{fo}|_{max}$; these trends are apparent in Fig. 10(a) when the eccentricity is 0.0. The case of the positive eccentricity $\varepsilon = 0.625$ is shown in Fig. 10(b), the $|C_{fi}|_{max}$ near $\theta = 15°$ and $|C_{fo}|_{max}$ near $\theta = 75°$. When

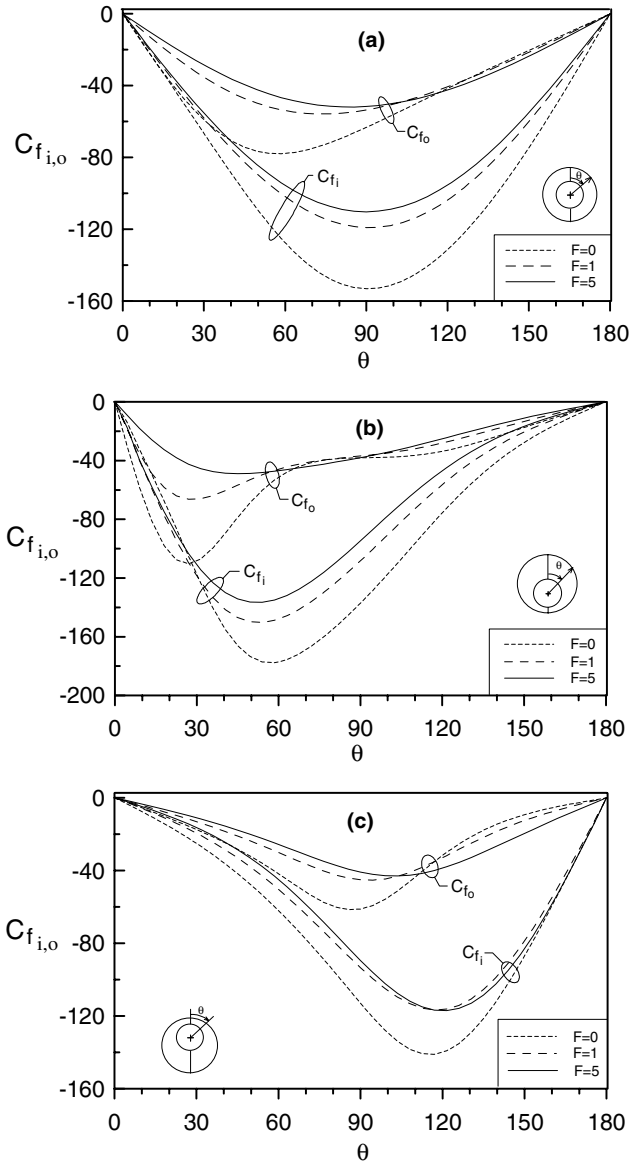

Fig. 9. Skin friction coefficient distribution on the inner and outer spheres for $R^* = 2.0$, $Pr = 0.7$ and $Ra = 10^3$ at different micropolar parameters $F = 0$, 1, 5: (a) $\varepsilon = 0.0$; (b) $\varepsilon = 0.625$; (c) $\varepsilon = -0.625$.

the negative eccentricity $\varepsilon = -0.625$ is shown in Fig. 10(c), the $|C_{fi}|_{max}$ near $\theta = 55°$ and $|C_{fo}|_{max}$ near $\theta = 90°$, besides, for the negative eccentricity, as $F = 0$ and 1, we find several peak values C_{fi} and C_{fo}, near $\theta = 15°$, which is exactly the position of second flow cell in the counterclockwise direction.

The circumferentially averaged Nusselt numbers at steady state obtained in the present study are given in Table 2, for various Rayleigh numbers in the three annular geometries and three different values of F under consideration. As the Rayleigh number increases beyond the conduction regime, the curves beyond the pseudoconduction region are straight lines on log–log coordinates. $\overline{Nu}$ can be correlated via a least square regression analysis in the form

$$\overline{Nu} = C\,Ra^m \tag{21}$$

for $Pr = 0.7$ and $R^* = 2.0$, where the constant values of C and m are listed in Table 3 for the three configurations and F values considered here.

Average Nusselt number $\overline{Nu}$ vs. Rayleigh number is plotted in Fig. 11 for a diameter ratio R^* of 2.0. When compared to the different eccentricity at fixed value of F. It reveals that the positive eccentricity can improve

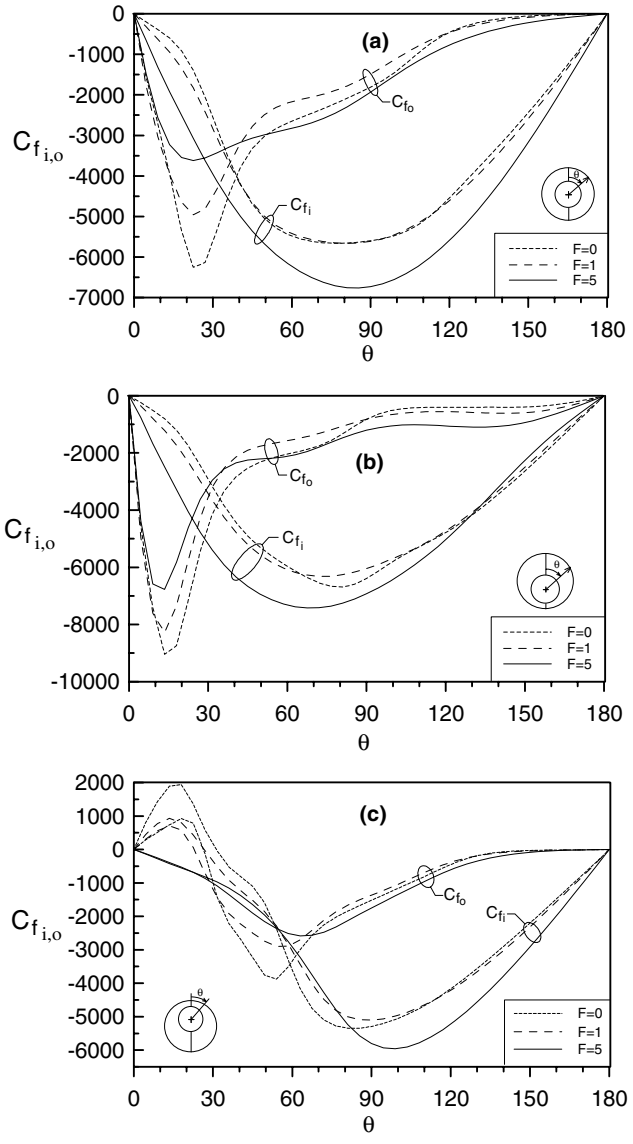

Fig. 10. Skin friction coefficient distribution on the inner and outer spheres for $R^* = 2.0$, $Pr = 0.7$ and $Ra = 10^5$ at different micropolar parameters $F = 0$, 1, 5: (a) $\varepsilon = 0.0$; (b) $\varepsilon = 0.625$; (c) $\varepsilon = -0.625$.

the average Nusselt number, but the negative eccentricity may not promote the convection effect. From other viewpoint with a fixed eccentricity compared to the different value of F, it visualizes that average Nusselt number $\overline{Nu}$ decreases with the increase of F at the overall Rayleigh number.

5. Conclusions

The transient natural convection using a micropolar fluid and Newtonian fluid in concentric and vertically eccentric spheres with isothermal boundary conditions have been analyzed numerically by a finite difference method. The transient developing series of the heat and fluid flow in the annuli have been visualized by means of contour maps of isotherms, streamlines and velocity vectors. Both the micropolar fluid and the Newtonian fluid in the positive eccentric geometric structure can enhance convective heat transfer rates, but the negative eccentric geometric structure provides the least favored circumstance for the development of natural convection between two spheres in the annulus. The average Nusselt number increases with Rayleigh number

Table 2
Average Nusselt number

ε	$R^* = 2.0$, $Pr = 0.7$					
	10^3	5×10^3	10^4	5×10^4	10^5	5×10^5
$F = 0$, $\overline{Nu}$ for Ra						
0.625	1.3338	1.7478	2.0230	2.9341	3.4620	–
0.000	1.1003	1.6341	1.9601	2.8906	3.3851	4.9147
−0.625	1.2464	1.5761	1.8091	2.6427	3.1887	–
$F = 1$, $\overline{Nu}$ for Ra						
0.625	1.2092	1.5746	1.7999	2.5842	3.0584	–
0.000	1.0309	1.3828	1.6916	2.5456	2.9874	4.3218
−0.625	1.1924	1.4166	1.6056	2.2733	2.7343	4.1606
$F = 5$, $\overline{Nu}$ for Ra						
0.625	1.1650	1.3700	1.5368	2.1350	2.4944	3.6949
0.000	1.0050	1.1069	1.3038	2.0732	2.4621	3.5272
−0.625	1.1432	1.2627	1.3783	1.8715	2.1833	3.3174

Table 3
Empirical constants and deviations for Eq. (20)

ε	C	m	Ra	Max. deviation (%)
$F = 0$				
0.625	0.30236	0.20971	10^3–10^5	3.49
0.000	0.20997	0.24126	10^3–5×10^5	1.18
−0.625	0.28377	0.20647	10^3–10^5	5.22
$F = 1$				
0.625	0.28662	0.20326	10^3–10^5	3.48
0.000	0.19389	0.23657	10^3–5×10^5	3.61
−0.625	0.26021	0.20516	10^3–10^5	9.97
$F = 5$				
0.625	0.28674	0.18924	10^3–10^5	9.03
0.000	0.19394	0.21807	10^3–5×10^5	1.30
−0.625	0.30188	0.17442	10^3–10^5	1.19

in each eccentricity displacement, but decreases with increasing F at fixed eccentricity for each Rayleigh number. From the micropolar parameter effect has been known that the heat transfer rate is lower for the micropolar fluid than that for the Newtonian fluid certainly. Under a low Rayleigh number, the skin friction force acting on the wall with the Newtonian fluid is stronger than that with the micropolar fluid. On the contrary, under a high Rayleigh number, the skin friction force acting on the outer spherical surface with the micropolar fluid is stronger than that with the Newtonian fluid evidently. According to the above results of numerical calculations can be applied to the realistic case of solar fluid heater. As the thermal energy storage cell is filled with micropolar fluid. It will be improving the thermal energy storage performance because it keeps warmer than the case that is filled with the Newtonian fluid.

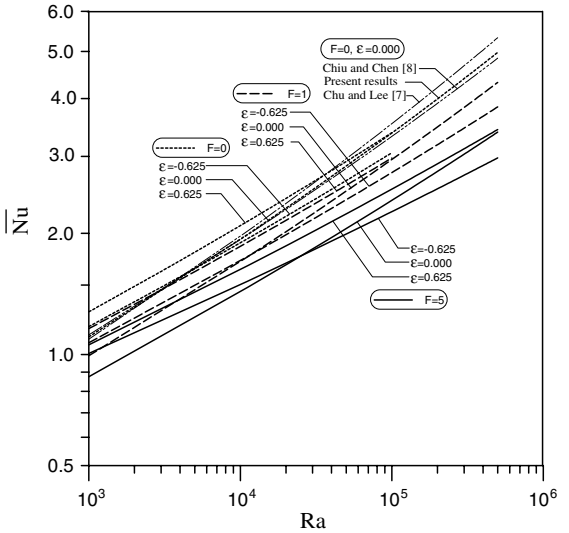

Fig. 11. Average Nusselt number as function of Rayleigh number for $Pr = 0.7$ and $R^* = 2.0$ at different micropolar parameters $F = 0$, 1, 5.

References

[1] E.H. Bishop, L.R. Mack, J.A. Scanlan, Heat transfer by natural convection between concentric spheres, Int. J. Heat Mass Transfer 9 (1966) 649–662.
[2] J.A. Scanlan, E.H. Bishop, R.E. Powe, Natural convection heat transfer between concentric spheres, Int. J. Heat Mass Transfer 13 (1970) 1857–1872.
[3] L.R. Mack, H.C. Hardee, Natural convection between concentric spheres at low Rayleigh numbers, Int. J. Heat Mass Transfer 11 (1968) 387–396.
[4] S.N. Singh, J. Chen, Numerical solution for free convection between concentric spheres at moderate Grashof numbers, Numer Heat Transfer 3 (1980) 441–459.
[5] K.N. Astill, H. Leong, R. Martorana, A numerical solution for natural convection in concentric spherical annuli, Proc. 19th Nat. Heat Tr. Conf. 8 (1980) 105–113.
[6] V.K. Garg, Natural convection between concentric spheres, Int. J. Heat Mass Transfer 35 (1992) 1935–1945.
[7] H.S. Chu, T.S. Lee, Transient natural convection heat transfer between concentric spheres, Int. J. Heat Mass Transfer 36 (1993) 3159–3170.
[8] C.P. Chiu, W.R. Chen, Transient natural convection heat transfer between concentric and vertically eccentric spheres, Int. J. Heat Mass Transfer 39 (1996) 1439–1452.
[9] C.P. Chiu, W.R. Chen, Transient natural convection between concentric and vertically eccentric spheres with mixed boundary conditions, Int. J. Heat Mass transfer 31 (1996) 137–143.
[10] A.C. Eringen, Simple microfluids, Int. J. Eng. Sci. 2 (1964) 205–217.
[11] A.C. Eringen, Theory of micropolar fluid, J. Math. Mech. 16 (1966) 1–18.
[12] A.C. Eringen, Theory of thermomicroluids, J. Math. Anal. Appl. 38 (1972) 480–495.

[13] T. Ariman, M.A. Turk, N.D. Sylvester, Microcontinuum fluid mechanics—A review, Int. J. Eng. Sci. 11 (1973) 905–930.
[14] S.K. Jena, S.P. Bhattacharyya, The effect of microstructure on the thermal convection in a rectangular box of fluid heated from below, Int. J. Eng. Sci. 24 (1986) 69–78.
[15] P.J. Roache, Computational Fluid Dynamics, Hermosa, Albuquerque, New Mexico, 1976.
[16] D.W. Peaceman, H.H. Rachford Jr., The numerical solution of parabolic and elliptic differential equations, J. Soc. Indust. Appl. Math. 3 (1) (1955) 28–41.
[17] S.P. Frankel, Convergence rates of iterative treatments of partial differential equations, Math Tables Other Aids Comput. 4 (1950) 65–67.
[18] D. Young, Iterative methods for solving partial differential equations of elliptic type, Trans. Am. Math. Soc. 76 (1954) 92–111.
[19] J.-P. Caltagirone, M. Combarnous, A. Mojtabi, Natural convection between two concentric spheres: transition toward a multicellular flow, Numer. Heat Transfer 3 (1980) 107–114.